

Star formation and dust extinction properties of local galaxies from AKARI-GALEX All-Sky Surveys:

First results from most secure multiband sample from FUV to FIR

T. T. Takeuchi¹, V. Buat², S. Heinis³, E. Giovannoli², F.-T. Yuan⁴, J. Iglesias-Páramo⁵, K. L. Murata⁴, and D. Burgarella²

¹ Institute for Advanced Research, Nagoya University, Furo-cho, Chikusa-ku, Nagoya 464–8601, JAPAN
e-mail: takeuchi@iar.nagoya-u.ac.jp

² Laboratoire d'Astrophysique de Marseille, OAMP, Université Aix-Marseille, CNRS, 38 rue Frédéric Joliot-Curie, 13388 Marseille cedex 13, FRANCE
e-mail: veronique.buat, elodie.giovannoli, denis.burgarella@oamp.fr

³ Department of Physics & Astronomy, The Johns Hopkins University, 3701 San Martin Drive, Baltimore, MD 21218, USA
e-mail: sebastien@pha.jhu.edu

⁴ Division of Particle and Astrophysical Sciences, Nagoya University, Furo-cho, Chikusa-ku, Nagoya 464–8602, JAPAN
e-mail: yuan.fangting, murata.katsushiro@g.mbox.nagoya-u.ac.jp

⁵ Instituto de Astrofísica de Andalucía (IAA, CSIC), Camino Bajo de Huétor 50, 18008 Granada, SPAIN
e-mail: jiglesia@iaa.es

ABSTRACT

Aims. We explore spectral energy distributions (SEDs), star formation, and dust extinction properties of galaxies in the Local Universe.

Methods. The AKARI All-Sky Survey provided the first bright point source catalog detected at 90 μm . Starting from this catalog, we selected galaxies by matching AKARI sources with those in the IRAS PSCz. Next, we have measured total GALEX FUV and NUV flux densities by a photometry software we have specifically developed for this purpose. Then, we have matched this sample with SDSS and 2MASS galaxies. By this procedure, we obtained the basic sample which consists of 776 galaxies. After removing objects with photometry contaminated by foreground sources (mainly in SDSS), we have defined the “secure sample” which contains 607 galaxies. Using this galaxy sample, we have explored various properties of galaxies related to star formation and dust extinction.

Results. The sample galaxies have redshifts $\lesssim 0.15$, and their 90- μm luminosities range from 10^6 to $10^{12} L_{\odot}$, with a peak at $10^{10} L_{\odot}$. The SEDs display a large variety, especially more than four orders of magnitude at M-FIR, but if we sort the sample with respect to 90 μm , their average SED shows a coherent trend: the more luminous at 90 μm , the redder the global SED becomes. The M_r -NUV- r color-magnitude relation of our sample does not show bimodality, and the distribution is centered on the green valley between the blue cloud and red sequence seen in optical surveys. We have established formulae to convert FIR luminosity from AKARI bands to the total infrared (IR) luminosity L_{TIR} . With these formulae, we calculated the star formation directly visible with FUV and hidden by dust. The luminosity related to star formation activity (L_{SF}) is dominated by L_{TIR} even if we take into account the far-infrared (FIR) emission from dust heated by old stars. At high star formation rate (SFR) ($> 20 M_{\odot} \text{yr}^{-1}$), the fraction of directly visible SFR, SFR_{FUV} , decreases. We also estimated the FUV attenuation A_{FUV} from FUV-to-total IR (TIR) luminosity ratio. We also examined the $L_{\text{TIR}}/L_{\text{FUV}}$ -UV slope (FUV – NUV) relation. The majority of the sample has $L_{\text{TIR}}/L_{\text{FUV}}$ ratios 5 to 10 times lower than expected from the local starburst relation, while some LIRGs and all the ULIRGs of this sample have higher $L_{\text{TIR}}/L_{\text{FUV}}$ ratios. We found that the attenuation indicator $L_{\text{TIR}}/L_{\text{FUV}}$ is correlated to the stellar mass of galaxies, M_{*} , but there is no correlation with specific SFR (SSFR), SFR/M_{*} , and dust attenuation $L_{\text{TIR}}/L_{\text{FUV}}$.

Conclusions. Together, these results show that the AKARI FIS All-Sky Survey gives a representative sample of SF galaxies in the Local Universe. This sample will be a comprehensive standard of various properties of SF galaxies to be compared with, e.g., high- z SF galaxies.

Key words. galaxies: evolution-galaxies: stellar content-infrared: galaxies-ultraviolet: galaxies

1. Introduction

Star formation history of galaxies is one of the most important and exciting topics in extragalactic astrophysics and observational cosmology. Especially, exploring the “true” absolute value of the cosmic star formation rate (hereafter SFR) has been of a central importance.

However, it remained difficult for a long time because of dust extinction. Even in the Local Universe, there are some prob-

lems to estimate the absolute value of SFR density because of different dependence of various SFR estimators on dust attenuation (e.g., Hopkins & Beacom, 2006, and references therein). Active star formation (SF) always comes along with dust production, because of various dust grain formation processes related to the final stage of stellar evolution (e.g., Dwek & Scalo, 1980; Dwek, 1998; Nozawa et al., 2003; Takeuchi et al., 2005c). Observationally, SFR of galaxies is measured by the ultraviolet (UV) luminosity from massive stars because of their short lifetime ($\sim 10^8$ yr) compared with the age of galaxies or the Universe. However, the UV photons are easily scattered and ab-

sorbed by dust grains. Hence the SFR of galaxies is always inevitably affected by dust which is produced by their SF activity. Since the absorbed energy is re-emitted at far-infrared (FIR) wavelengths, it is essential to observe galaxies both at UV and FIR to have an unbiased view of their SF (e.g., Buat et al., 2005; Seibert et al., 2005; Cortese et al., 2006; Takeuchi et al., 2005a).

To know the history of SFR in the Universe, we must know the starting reference value, i.e., the SFR density in the Local Universe: otherwise, we cannot define how much larger the SFR was in the past. However, since the volume of the Local Universe is limited by definition, an all-sky survey is the only viable way to refine our knowledge of local galaxies. On the “directly visible SF” side, the advent of the UV surveyor-type satellite GALEX (Martin et al., 2005) has changed the situation of UV astronomy drastically. GALEX is performing an all-sky survey (All Sky Imaging Survey: AIS) at FUV (1530 Å) and NUV (2300 Å) with detection limits of 19.9 and 20.8 mag (Morrissey et al., 2007), as well as deep surveys in some selected regions. In a previous study, we have shown that GALEX AIS provides us with an unprecedented opportunity to explore the visible SF in the Local Universe (Buat et al., 2007a).

As for the “hidden” side of SF, the Infrared Astronomical Satellite (IRAS; Neugebauer et al., 1984) has brought a vast amount of statistics of dusty galaxies in the Local Universe by IRAS Point Source Catalog (PSC) (see, e.g., Soifer et al., 1987). Subsequently, FIR facilities with much higher sensitivity have been launched, like ISO (e.g., Genzel & Cesarsky, 2000; Verma et al., 2005) and Spitzer (e.g., Soifer et al., 2008), and revealed the deep IR universe, but the latter two were observatories dedicated to pointed observations.

In contrast to the latter two facilities, the Japanese IR satellite AKARI has performed various large-area surveys at IR wavelengths (Murakami et al., 2007) after IRAS, *especially including all-sky surveys at FIR and MIR*. In particular, with the aid of the Far-Infrared Surveyor (FIS; Kawada et al., 2007) onboard, various IR surveys were performed by AKARI. AKARI FIS has four FIR wavebands centered on 65, 90, 140, and 160 μm , and a FIR all-sky survey was completed by this instrument. Since the latter two bands are longer than 100 μm which was the longest wavelength band of IRAS, the obtained sample of dusty galaxies is less biased than the IRAS sample, i.e., thanks to the better sensitivity to cooler dust than IRAS, AKARI can detect galaxies with dust emission with lower temperatures. Thus, AKARI is a very promising facility to bring new knowledge of galaxies with cold dust. In addition to these SF-related wavelengths, we need other various wavelength bands to examine physical properties of galaxies, e.g., stellar mass [closely related to near-IR (NIR)], and intermediate stellar population (related to optical). For the former, we have a set of all-sky data from 2-Micron All-Sky Survey (2MASS; Skrutskie et al., 2006), and for the latter, the SDSS final data (DR7) are publicly available¹, even if SDSS is not an all-sky survey.

In this work, we constructed a multiband galaxy catalog based on AKARI All-Sky Survey 90- μm selected sources associated with IRAS PSCz galaxies (Saunders et al., 2000). Then, we measured GALEX FUV and NUV flux densities, and associated SDSS and 2MASS photometries. For this initial study, we have only selected “secure” galaxies with good photometric measurements for most of the bands. We present the sample construction in Section 2. We describe basic properties of galaxies in the sample in Section 3. Results on the SF and dust attenuation

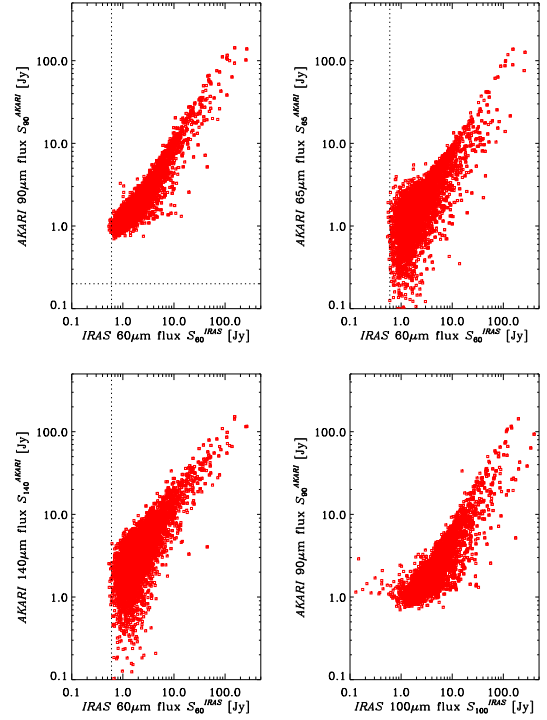


Fig. 1. Comparison between AKARI FIS and IRAS PSCz flux densities. Upper-left, upper-right, and lower-left panels present comparisons of IRAS 60 μm with AKARI 90 μm , 65 μm , and 140 μm flux densities of the AKARI-IRAS correlated sample. The vertical dotted lines in these panels represent the flux density limit of IRAS PSCz. Lower-right panel shows a comparison of IRAS 100 μm with AKARI 90 μm flux densities. The horizontal dotted line in Upper-left panel represents the formally expected detection limit of FIS 90 μm .

are presented in Section 4. Section 5 is devoted to our summary and conclusions.

Throughout the paper we will assume $\Omega_{\text{M}0} = 0.3$, $\Omega_{\Lambda 0} = 0.7$ and $H_0 = 70 \text{ km s}^{-1} \text{ Mpc}^{-1}$. The luminosities are defined as νL_ν and expressed in solar units assuming $L_\odot = 3.83 \times 10^{33} \text{ erg s}^{-1}$.

2. Sample construction

2.1. Construction of the parent FIR sample from AKARI and IRAS PSCz

2.1.1. AKARI FIS All-Sky Survey

The primary purpose of the AKARI mission is to provide second-generation infrared (IR) catalogs with better spatial resolution and wider spectral coverage than the IRAS catalog. AKARI is equipped with a cryogenically cooled telescope of 68.5 cm aperture diameter and two scientific instruments, the Far-Infrared Surveyor (FIS; Kawada et al., 2007) and the Infrared Camera (IRC; Onaka et al., 2007). Among various astronomical observations performed by AKARI, as we have mentioned in Introduction, an all sky survey with FIS has been carried out (AKARI All-Sky Survey). Since FIS is an instrument dedicated to FIR $\lambda = 50\text{--}180 \mu\text{m}$, all the AKARI FIS bands are in the FIR wavelengths: *N60* (65 μm), *WIDE-S* (90 μm), *WIDE-L* (140 μm), and *N160* (160 μm) (Kawada et al., 2007). Hereafter, we note as S_{65} , S_{90} , S_{140} and S_{160} the flux densities in these bands. Especially, since FIS has sensitivity at longer

¹ URL: <http://www.sdss.org/dr7/>.

wavelengths than IRAS, a new classification scheme is needed if we try to select a certain class of objects. Such a scheme is not merely an empirical technique but also will provide us with a new understanding of objects with cool dust which were difficult to detect by IRAS bands.

We use the AKARI FIS Bright Source Catalogue (BSC), the first primary catalog from the AKARI All-Sky Survey. Data from the β -1 version of this catalog are used in this work. AKARI BSC is supposed to have a uniform detection limit, corresponding to per scan sensitivity, over the entire sky, except for very bright sky parts where different data acquisition mode had to be applied. A summary of the All-Sky Survey is presented in Yamamura et al. (2009). The AKARI FIS BSC provides data for 64311 sources. For each detected source, AKARI source identifier, equatorial coordinates of the source position and flux densities in the four FIR bands are given. Errors are not estimated for each individual source, but instead they are in total estimated to be 35 %, 30 %, 60 %, and 60 % at $N60$, $WIDE-S$, $WIDE-L$, and $N160$, respectively (Yamamura et al., 2008). AKARI IRC performed another all sky survey, but the data are not fully reduced at the time we have been preparing this paper. Hence we focus on the FIS data only.

2.1.2. Matching with IRAS PSC_z

The AKARI BSC contains many Galactic sources, like AGBs, HII regions, planetary nebulae, etc. (e.g., Pollo et al., 2010). In order to construct a reliable catalog of galaxies, we should pick up FIS sources confirmed as galaxies. For this purpose, we have performed a cross identification of BSC sources with the IRAS PSC_z (Saunders et al., 2000). The PSC_z is a redshift survey of galaxies selected at IRAS 60 μ m with a flux density limit of $S_{60} > 0.6$ [Jy]². The PSC_z contains ~ 16000 galaxies. We have put a limit on recession velocity $v > 1000$ km s⁻¹ so that we can avoid the effect of the peculiar velocity of galaxies. Then, we have matched the AKARI BSC sources with PSC_z galaxies with a search radius of 36 arcsec, which corresponds to the position uncertainty of IRAS PSC. The number of matched sources was 5890. To examine the effect of the choice of search radius, we changed the criterion from 20–60 arcsec. This change of radius does not have a significant impact on the resulting catalog (≤ 5 %). Hence, we use the catalog with a search radius of 36 arcsec in the following analysis.

For further analysis, we make a cross identification with SDSS galaxies (see Sec. 2.3). Then, we have to restrict our data only to the area covered by SDSS DR7 which is 8378.015 deg². This restriction to this region of the sky has one advantage: the Galactic diffuse FIR emission is strong in some areas of the sky. In such regions, measured FIR flux densities of point sources are contaminated by the Galactic emission and not very accurate. Since the SDSS region is selected so that the Galactic extinction is small, the selected area automatically avoids such FIR-bright regions. Then, by this selection, our sample automatically excludes strongly contaminated sources. The resulting parent catalog contains 1186 galaxies.

2.1.3. Flux density comparison between AKARI and IRAS

We compared AKARI and IRAS flux densities to examine our sample selection. The correlation is shown in Figure 1. The hori-

zontal dotted lines in upper-left, upper-right, and lower-left panels represent the flux density limit of IRAS PSC_z. AKARI BSC sources are selected at $WIDE-S$, i.e., 90 μ m. It is important to see which selection controls the sample selection. As seen in the upper-left panel, the IRAS PSC_z limit and AKARI limit are both well-defined, and neither of them strongly restricts the sample. The effective 90 μ m flux density limit of our parent sample is ~ 0.8 Jy.

2.2. GALEX photometry

GALEX AIS now observed 25000 deg² at FUV and NUV. The latest version of the public imaging is GR4/GR5³. We have measured the FUV and NUV photometry of the parent AKARI galaxies as follows:

1. Cut out a 30' \times 30' square subimage from GALEX AIS images around each AKARI galaxy.
2. Select a subimage with the largest exposure time when multiple observations were available.
3. Measure FUV and NUV flux densities. The NUV observation is taken as our reference.

Since the sky coverage of GALEX AIS is not complete, in some cases we do not have a proper GALEX image for an AKARI galaxy. In such a case we omit the galaxy because we do not have any UV information.

Almost all of the sources are resolved by GALEX. They are thus very often separated into small bright patchy regions, and the GALEX pipeline misidentifies these fragments as individual objects. This is referred to as *shredding*. We must deal with the shredding to obtain sensible flux density measurements for nearby extended galaxies. For this purpose, we have used an IDL software package developed by ourselves. This software performs aperture photometry in the NUV sub-image using a set of elliptical apertures. Total flux density is calculated within the aperture corresponding to the convergence of the growth curve. The sky background is measured by combining several individual regions around the source. NUV and FUV flux densities are corrected for Galactic extinction using the Schlegel map (Schlegel et al., 1998) and the Galactic extinction curve of Cardelli et al. (1989). A detailed description of the photometry process can be found in Iglesias-Páramo et al. (2006).

This software was already used for our previous IRAS-GALEX based studies (Buat et al., 2007a), and its performance is carefully checked and established. During the procedure, we also excluded all the sources contaminated by stars or too close to be disentangled by the photometry software. By this procedure, the number of remaining galaxies is 776.

2.3. Matching with SDSS and 2MASS galaxies

We further matched the AKARI-IRAS PSC_z-GALEX sample (776 galaxies, hereafter abbreviated as the AKARI-GALEX sample) with SDSS and 2MASS.

The AKARI-GALEX sample was matched with the 2MASS All-Sky Extended Source (XSC) catalog in order to obtain the NIR (J , H , and K_s) flux densities. A matching radius of 20'' was initially adopted for the cross correlation. All but 7 out of the 776 galaxies in the AKARI-GALEX sample showed 2MASS counterparts at distances closer than the matching radius. In case of multiple candidates, we always selected the brightest one at K_s band as the most plausible one. A further cross correlation with

² Because of this step, we should note that we do not make a maximal use of the advantage of the long wavelength bands of AKARI FIS, since the sample is limited by IRAS bands ($\lambda < 100$ μ m).

³ URL: <http://galex.stsci.edu/GR4/>

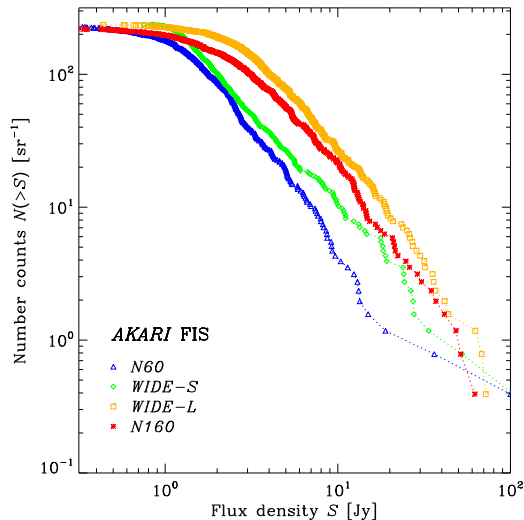


Fig. 2. Number counts of our AKARI multiband sample at AKARI FIS four bands. Triangles, diamonds, squares, and crosses represent AKARI *N60*, *WIDE-S*, *WIDE-L*, and *N160* galaxy counts, respectively.

a matching radius of $30''$ was attempted for these seven galaxies with no 2MASS counterpart within the $20''$ radius. However, again, no 2MASS counterparts were found, and we adopted the standard 2MASS XSC upper limits for these galaxies at *J*, *H*, and *Ks* bands. The standard 2MASS limiting magnitudes at *J*, *H*, and *Ks* are 14.7, 13.9 and 13.1 mag, respectively (Jarrett et al., 2000).

We also matched the AKARI-GALEX sample to SDSS using the GALEX coordinates for the AKARI-GALEX objects, and a search radius of $15''$. In the case of SDSS, large resolved galaxies such as those we are dealing with here are shredded in multiple detections during the deblending step of the pipeline. We used the closest SDSS match to the AKARI object to obtain the SDSS photometry of the parent object, namely the object detected by the SDSS pipeline before deblending. We inspected all sources to check that the actual flux measured for the parent object is not contaminated by nearby bright stars, artifacts etc.

For most of the sample galaxies, SDSS galaxies were associated. However, stars superposed on the SDSS galaxy images often hamper accurate photometry. It requires a very careful masking of the SDSS image, and in the current analysis we simply omitted such galaxies. After this selection, 607 galaxies remained. We call this sample “the final sample”. Almost all galaxies have very secure photometric data at UV, optical, NIR, MIR, and FIR, as well as the redshift information.

3. Basic Properties of the Sample Galaxies

3.1. Number counts

Figure 2 presents the cumulative AKARI flux density distribution (number counts) of our final sample. We see that the flux density limit of the sample at $90\ \mu\text{m}$ is $\sim 1\ \text{Jy}$, shallower than the original limit of $\sim 0.8\ \text{Jy}$, because of additional constraints to have optical–NIR counterparts.

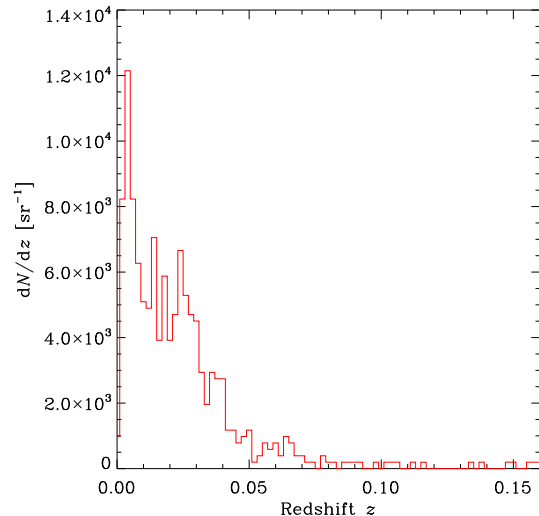


Fig. 3. Redshift distribution of the sample. The distribution is normalized so that we obtain the number of galaxies per unit solid angle if we integrate it over redshifts.

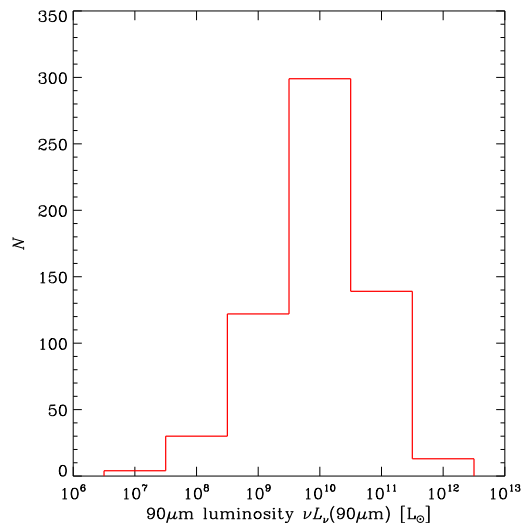


Fig. 4. Luminosity distribution of the sample at $90\ \mu\text{m}$.

3.2. Redshift and luminosity distributions

The redshift distribution of our final sample is shown in Figure 3. Since AKARI FIS BSC is rather shallow, most of the sample locate at low redshifts $z \lesssim 0.05$. This is quite consistent with predictions of various IR galaxy evolution models (e.g., Takeuchi et al., 2001a,b; Chary & Elbaz, 2001).

Figure 4 presents the $90\text{-}\mu\text{m}$ luminosity distribution of the sample. Since this is a raw luminosity distribution of IR galaxies, it decreases toward the faint end. The $90\text{-}\mu\text{m}$ luminosity ranges from $10^6 L_\odot$ – $10^{12} L_\odot$. Only a few galaxies are classified as ultraluminous IR galaxies (ULIRGs). The peak of the luminosity distribution is around $10^{10} L_\odot$, which is more luminous than the knee of the $60\text{-}\mu\text{m}$ luminosity function (Takeuchi et al., 2003a). Since our selection procedure is multifold and complicated, estimating a reliable luminosity function is not straightforward. We will try this task in future works.

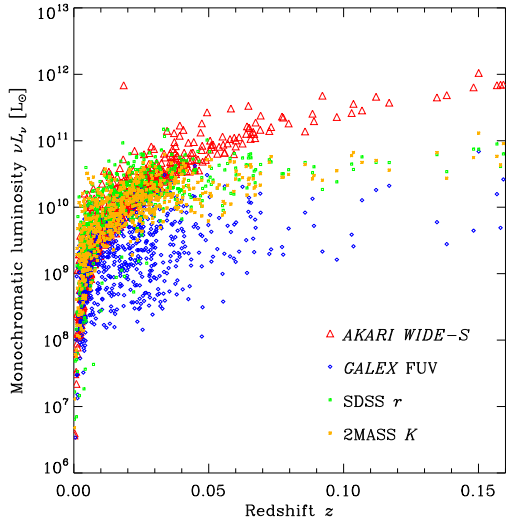


Fig. 5. Luminosity distribution of the sample at several wavelengths. Triangles, diamonds, squares, and crosses represent galaxies AKARI *WIDE-S*, GALEX FUV, SDSS *r*, and 2MASS *K*-band, respectively.

We can compare the distribution of galaxies on the redshift–luminosity plane to see the effect of the shape of luminosity function. We show the z - νL_ν relation in Figure 5. Some representative wavelengths are shown: AKARI *WIDE-S*, GALEX FUV, SDSS *r*, and 2MASS *Ks*. We see that the luminosity at 90 μm increases monotonically toward higher redshifts, while the optical and near-IR (NIR) luminosities of the same galaxies saturate at certain values. This is related to the difference in the shape of their luminosity functions (see, e.g., Takeuchi et al., 2005a; Iglesias-Páramo et al., 2006); i.e., the luminous end of the function exponentially declines at optical-NIR and UV, while it shows a power-law decline at FIR. This is also related to the fact that the more luminous galaxies are more strongly extinguished by dust. We will revisit this issue in a much more direct way in Section 4.4

3.3. SEDs of the sample

Since we have the monochromatic luminosities from FUV to FIR, we construct the spectral energy distributions (SEDs) of our sample. We show all the SEDs of the sample in Figure 6. Large empty squares represent the AKARI FIS measurements, while the small squares represent all the other data in Figure 6. We observe a very large variety of SEDs among the sample galaxies.

To see a global trend of the SEDs more clearly, we sorted the sample by their 90- μm luminosities and subdivided the sample into six logarithmic bins from $10^6 L_\odot$ to $10^{12} L_\odot$ (with a bin width $\Delta \log L_{90} = 1$). By taking an average and median, we constructed “average SEDs” as a function of 90- μm luminosity, shown in Figure 7. Because of a large dispersion and asymmetric distribution of the SEDs in each bin, sometimes the average and median SEDs do not agree very well. Even so, now the trend is more clearly seen: low 90- μm luminosity galaxies have cooler dust emission and bluer UV-optical continuum, while high 90- μm luminosity galaxies have hotter dust emission and redder UV-optical continuum.

The 90- μm luminosity dependence of the dust emission temperature is more clearly seen if we plot a flux density ratio

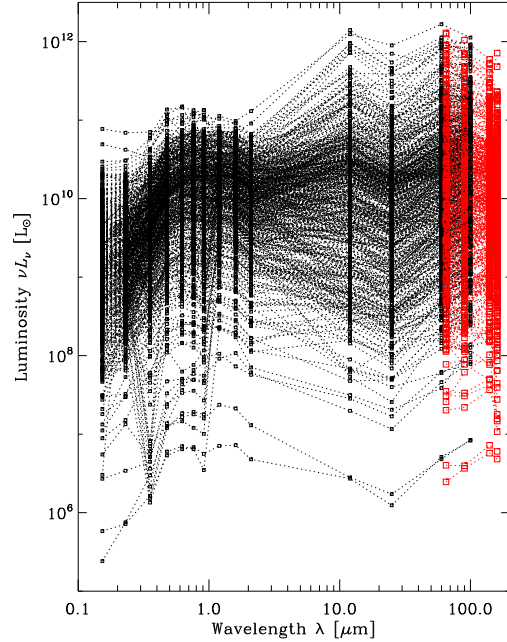


Fig. 6. Spectral energy distributions (SEDs) of the whole sample. Large empty squares represent the AKARI measurements, while the small squares are data taken from GALEX FUV, GALEX NUV, SDSS *u*, *g*, *r*, *i*, *z*, 2MASS *J*, *H*, *Ks*, and IRAS 12, 25, 60, and 100 μm from left to right. Dotted lines connect data points of each object to guide the eye.

S_{65}/S_{90} as a function of L_{90} . This is shown in Figure 8. Again, the agreement between average and median values is not excellent, we see a clear monotonically increasing trend of the flux density ratio along with L_{90} .

The lowest luminosity galaxies have the largest uncertainty mainly because of poor statistics. This problem will be solved by constructing deeper and larger sample, possibly by the next generation AKARI FIS catalog. The most 90- μm luminous galaxies seem to have an upturn at UV. This may be because of an AGN component in these galaxies. We will examine this issue in our future work. In both Figures 6 and 7, it is clear that AKARI FIS measurements at *N60* and *WIDE-S* do not agree with IRAS ones. This discrepancy is mostly due to the better angular resolution of AKARI FIS compared with IRAS. Thus, the measured values are much less contaminated by Galactic cirrus emission. Also because of better angular resolution, the source confusion effect is much smaller than for IRAS. As both cirrus and source confusion effects cause flux boosting for IR galaxy number counts, the IRAS flux densities could be overestimated (Takeuchi & Ishii, 2004). Jeong et al. (2007) also examined the same problem with an early AKARI sample and concluded that the difference between IRAS and AKARI flux densities are due to the confusion effects. We see a strange bump at 12 μm for luminous galaxies. This may not be a physical feature in the SEDs of our sample but because of a poor measurement at this band by IRAS. In the redshift–luminosity diagram at 12 μm (see Fig. A.1), we see that many galaxies locate on the limiting luminosity line. This means that, even if they are classified as measurements, actually they are upper limits of the flux density. We plan to study this point further by AKARI IRC all-sky survey in the future.

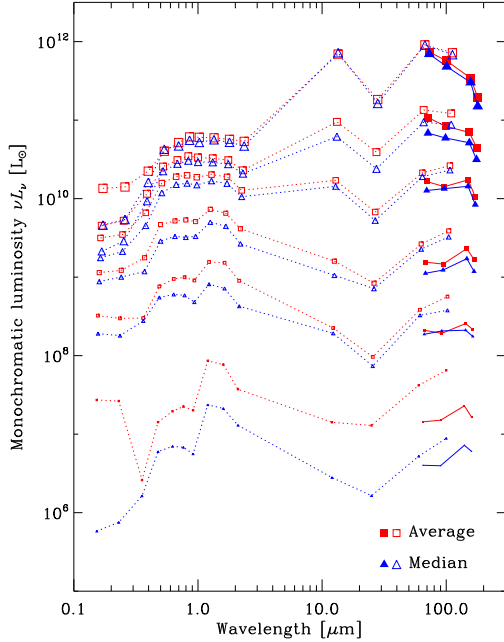


Fig. 7. Averaged spectral energy distributions of our sample as a function of $90 \mu\text{m}$ luminosity. Luminosity bins used here are the same as the bins in Figure 4. The central luminosities of the bins are 10^7 , 10^8 , 10^9 , 10^{10} , 10^{11} , and $10^{12} L_{\odot}$, respectively, and the obtained average SEDs are represented with different size of the symbols: from the smallest corresponding to $10^7 L_{\odot}$ to the largest corresponding to $10^{12} L_{\odot}$. Filled and empty squares are averaged SEDs, while filled and empty triangles are median SEDs.

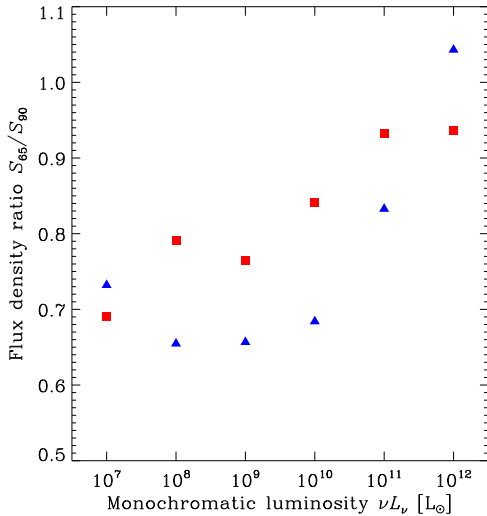


Fig. 8. Dependence of the flux density ratio S_{65}/S_{90} on average $90\text{-}\mu\text{m}$ luminosity. Same as Fig. 7, the squares are estimated from averaged SEDs, while triangles are from median SEDs.

3.4. The $\text{NUV} - r$ distribution

The $\text{NUV} - r$ restframe color is very efficient to separate the galaxies into blue and red populations (Salim et al., 2007; Martin et al., 2007). At high- z , IR selected galaxies observed with Spitzer were found to populate the so-called green valley

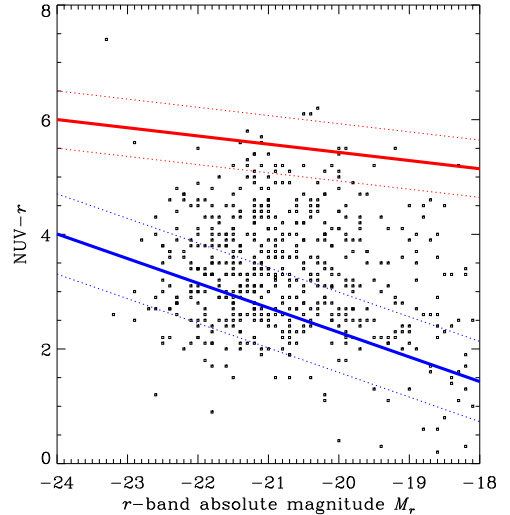


Fig. 9. The absolute r -magnitude- $\text{NUV} - r$ color distribution. Upper and lower thick solid lines represent the average red sequence and blue cloud taken from Salim et al. (2007), with its envelope indicated by dotted lines.

between the blue cloud and red sequence, first mentioned by Bell et al. (2005) and further identified in the COSMOS fields (Kartaltepe et al., 2009; Vergani et al., 2009).

However, in contrast, no systematic study of IR selected galaxies has been performed in the nearby universe until now. Figure 9 shows the distribution of the $\text{NUV} - r$ color for our sample galaxies against the absolute magnitude at r -band, M_r . The distribution in $\text{NUV} - r$ is found to be large and monolithic in contrast to the bimodal distribution found in optical surveys. From Figure 1 of Salim et al. (2007) (based on an SDSS-GALEX selected sample), we approximate the red sequence on this diagram with a linear relation

$$\text{NUV} - r = -0.143M_r + 2.57, \quad (1)$$

with ± 0.5 envelopes, and the blue cloud with

$$\text{NUV} - r = -0.429M_r - 6.29, \quad (2)$$

with ± 0.7 . Clearly, we see that our galaxies lie in the blue cloud and populate the green valley to produce a continuous distribution, and only a few objects are located in the red sequence. Therefore, the color distribution of FIR-selected galaxies is different than the one obtained from an optical selection, as they preferentially populate the green valley between the red sequence and blue cloud. An interpretation of this behavior in terms of dust attenuation, SF history or AGN activity will be developed in a future paper.

4. Star Formation and Dust Extinction of the $90 \mu\text{m}$ -Selected Galaxies

4.1. Total dust luminosity from AKARI FIS bands

To calculate SF- and attenuation-related physical properties of the galaxies, a total IR (TIR) luminosity is required. Various estimators of L_{TIR} were proposed by previous authors (Helou et al., 1988; Dale et al., 2001; Dale & Helou, 2002; Sanders & Mirabel, 1996). Takeuchi et al. (2005b) has shown

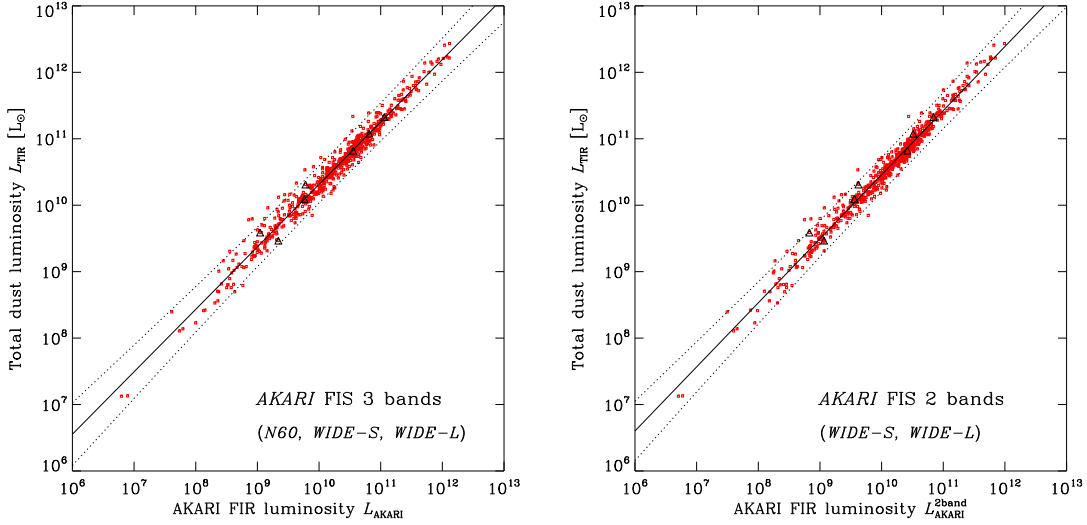


Fig. 10. Relation between the AKARI FIR luminosity and total IR (TIR) luminosity of the sample. Left panel is for the AKARI FIR luminosity defined by eq. (4), while right panel is for the AKARI FIR luminosity from 2 bands, defined by eq. (8). Black solid lines are the best least-square fits to the data, and the dotted curves represent the 95 % confidence levels of the lines. Triangles are galaxies with IRAS 100 μm quality flag larger than 3, i.e., those with insecure flux density measurement.

that we can safely estimate the TIR luminosity by a formula proposed by Sanders & Mirabel (1996):

$$L_{\text{TIR}} \equiv 4.93 \times 10^{-22} [13.48L_{\nu}(12\mu\text{m}) + 5.16L_{\nu}(24\mu\text{m}) + 2.58L_{\nu}(60\mu\text{m}) + L_{\nu}(100\mu\text{m})] [L_{\odot}]. \quad (3)$$

Since our sample contains all IRAS band flux densities, we can use the estimator of Sanders & Mirabel to examine the AKARI FIR flux. In this subsection, we make an attempt to establish a reliable formula to convert a FIR luminosity measured by AKARI to the TIR luminosity.

Since AKARI FIS has continuous bands from $\sim 50 \mu\text{m}$ to $\sim 160 \mu\text{m}$, we can easily define FIR flux simply by adding the flux densities multiplied with their bandwidths (in [Hz]). Hirashita et al. (2008) has defined the AKARI FIR luminosity as

$$L_{\text{AKARI}} = \Delta\nu(N60) L_{\nu}(65 \mu\text{m}) + \Delta\nu(WIDE-S) L_{\nu}(90 \mu\text{m}) + \Delta\nu(WIDE-L) L_{\nu}(140 \mu\text{m}), \quad (4)$$

where

$$\Delta\nu(N60) = 1.58 \times 10^{12} [\text{Hz}] \quad (5)$$

$$\Delta\nu(WIDE-S) = 1.47 \times 10^{12} [\text{Hz}] \quad (6)$$

$$\Delta\nu(WIDE-L) = 0.831 \times 10^{12} [\text{Hz}]. \quad (7)$$

However, since the sensitivity of AKARI *N60* is not as good as other two wide bands, if we can use FIR luminosity defined only by *WIDE-S* and *WIDE-L*, it will be useful because we can have larger number of galaxies. We define $L_{\text{AKARI}}^{2\text{band}}$ by omitting the term of *N60* as

$$L_{\text{AKARI}}^{2\text{band}} = \Delta\nu(WIDE-S) L_{\nu}(90 \mu\text{m}) + \Delta\nu(WIDE-L) L_{\nu}(140 \mu\text{m}). \quad (8)$$

Figure 10 presents correlations between L_{AKARI} and L_{TIR} . Left panel shows the correlation between L_{AKARI} of Hirashita et al. (2008) and L_{TIR} , while right panel shows the one between $L_{\text{AKARI}}^{2\text{band}}$ and L_{TIR} . The fitting results are as follows:

$$\log L_{\text{TIR}} = 0.940 \log L_{\text{AKARI}} + 0.914, \quad (9)$$

$$r = 0.987, \quad (10)$$

and

$$\log L_{\text{TIR}} = 0.964 \log L_{\text{AKARI}}^{2\text{band}} + 0.814, \quad (11)$$

$$r = 0.989, \quad (12)$$

where r is the correlation coefficient. The solid lines in Figure 10 depict these equations. The envelopes delineated by dotted lines in Figure 10 represent the 95 % confidence intervals.

In some cases the quality of IRAS 100 μm flux density measurement is poor; we examine the impact of these objects in Figure 10. Triangles represent galaxies with IRAS 100 μm quality flag larger than 3, i.e., the ones for which the measurement was difficult and not secure. However, even so, clearly they lie well within the distribution of the whole sample and do not have a significant impact on the statistical analysis.

Since these plots present luminosity-luminosity correlations, the very tight correlations are not extremely surprising. However, uncertainties of these equations are within a factor of $\sim 2-3$, which means that the estimation works very well even if we do not have MIR measurements. We also stress that the correlation is even better if we only use AKARI wide bands.

Hereafter, we use the total IR luminosity L_{TIR} obtained from AKARI *N60*, *WIDE-S*, and *WIDE-L* [equation (9)] for all the following analysis. *Namely, when we mention L_{TIR} , it is always AKARI-based total IR luminosity.*

4.2. Luminosity from current star formation

Now we can compare the FUV (L_{FUV}) and total IR (TIR) (L_{TIR}) luminosities for our final sample. This is shown in Figure 11. It is striking that the luminosity is dominated by L_{TIR} for the vast majority of our sample, even though we take into account that they are FIR-selected. Also, it is worth mentioning that the luminosity at FUV does not exceed $10^{11} L_{\odot}$. In contrast, L_{TIR} can be much higher.

By combining L_{FUV} and L_{TIR} , we can define the luminosity contribution from newly formed stars, L_{SF} :

$$L_{\text{SF}} \equiv L_{\text{FUV}} + (1 - \eta)L_{\text{TIR}}, \quad (13)$$

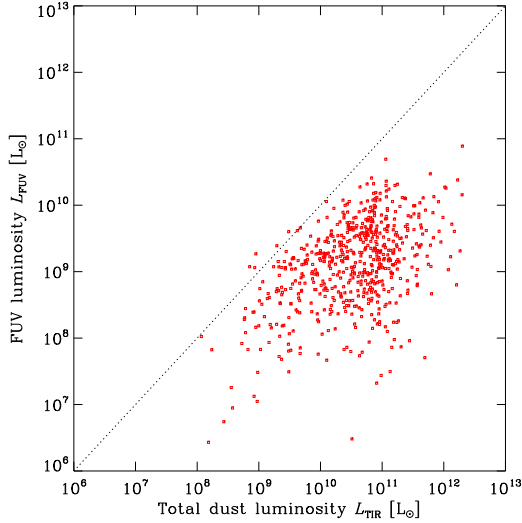


Fig. 11. Comparison between TIR and FUV luminosities. The diagonal dotted line represents the case if L_{TIR} equals L_{FUV} .

where η is the fraction of the dust emission due to the heating of grains by old stars which is not directly related to the recent SFR. We adopt a value of 30 % for this fraction (Hirashita et al., 2003). The contribution of L_{FUV} and L_{TIR} is shown in Figure 12. Naturally, the contribution of $(1 - \eta)L_{\text{TIR}}$ dominates L_{SF} . In contrast, the contribution of L_{FUV} has a very large scatter, and the correlation is very poor. Hence, it is not surprising that it is very difficult to estimate the total energy emitted by newly formed stars only from FUV information, even in an average sense. The UV contribution becomes significant at lower luminosities $L_{\text{SF}} < 10^{10} L_{\odot}$, as seen in the left panel of Figure 12.

4.3. Star formation rate of galaxies in our sample

Here, we interpret the data in terms of SFR. Assuming a constant SFR over 10^8 yr, and Salpeter initial mass function (IMF) (Salpeter, 1955, mass range: 0.1–100 M_{\odot}), we have the relation between the SFR and L_{FUV}

$$\log \text{SFR}_{\text{FUV}} = \log L_{\text{FUV}} - 9.51. \quad (14)$$

For the IR, to transform the dust emission to the SFR, we assume that all the stellar light is absorbed by dust. Then, we obtain the following formula under the same assumption for both the SFR history and the IMF as those of the FUV,

$$\log \text{SFR}_{\text{dust}} = \log L_{\text{TIR}} - 9.75 + \log(1 - \eta). \quad (15)$$

Here, again, η is the fraction of the dust emission by old stars. Thus, the total SFR is simply

$$\text{SFR} = \text{SFR}_{\text{FUV}} + \text{SFR}_{\text{dust}}. \quad (16)$$

The obtained SFR is shown as a function of the fraction of the contribution of SFR_{FUV} in Figure 13. Reflecting the large scatter of $L_{\text{FUV}}/L_{\text{SF}}$, the scatter of $\text{SFR}_{\text{FUV}}/\text{SFR}$ is very large at $\text{SFR} < 20 M_{\odot} \text{ yr}^{-1}$. However, quite sharply, no galaxies have a large contribution of SFR_{UV} at $\text{SFR} > 20 M_{\odot} \text{ yr}^{-1}$. The vertical dotted line shows this “threshold” SFR in Figure 13.

4.4. Dust attenuation

4.4.1. Dust attenuation of the sample

Galaxies selected in IR are expected to have a quite large dust attenuation. Here we examine the extinction properties of galaxies in the sample. For this study, a good observational indicator of dust attenuation is required. The $L_{\text{TIR}}/L_{\text{FUV}}$ ratio is widely recognized to be a robust measure of dust attenuation. This ratio was found to increase with the star formation luminosity in a similar way from $z = 0$ to $z = 0.7$ (Martin et al., 2005; Buat et al., 2007b; Zheng et al., 2006). Dust attenuation can be derived using the formula of Buat et al. (2005):

$$\begin{aligned} A_{\text{FUV}} = & -0.0333 \left(\log \frac{L_{\text{TIR}}}{L_{\text{FUV}}} \right)^3 \\ & + 0.3522 \left(\log \frac{L_{\text{TIR}}}{L_{\text{FUV}}} \right)^2 \\ & + 1.1960 \left(\log \frac{L_{\text{TIR}}}{L_{\text{FUV}}} \right) + 0.4967 \text{ [mag]}. \end{aligned} \quad (17)$$

Figure 14 presents the variation of $L_{\text{TIR}}/L_{\text{FUV}}$ as a function of the star formation luminosity. A clear increase of $L_{\text{TIR}}/L_{\text{FUV}}$ with L_{SF} is seen. The solid line is the mean trend of local galaxies found in our IRAS study (Buat et al., 2007a):

$$\log \left(\frac{L_{\text{TIR}}}{L_{\text{FUV}}} \right) = 0.64 \log L_{\text{SF}} - 5.5. \quad (18)$$

This line was estimated by a weighting of $L_{\text{TIR}}/L_{\text{FUV}}$ with $1/V_{\text{max}}$ to eliminate the flux selection effect, i.e., the effect that more luminous galaxies can be more easily detected. In contrast, we plot raw values of $L_{\text{TIR}}/L_{\text{FUV}}$. However, though the steep rise of the distribution of $L_{\text{TIR}}/L_{\text{FUV}}$ with L_{SF} is partially because of this selection effect, the trend is still well consistent with our IRAS study (Buat et al., 2007a), and the conclusion would remain valid.

4.4.2. Dust attenuation versus the slope of the UV continuum

The slope of the UV continuum is commonly used as a proxy to estimate dust attenuation and $L_{\text{TIR}}/L_{\text{FUV}}$ when IR data are not available or considered as unreliable (Daddi et al., 2007; Reddy et al., 2008; Reddy & Steidel, 2009). This method is based on a calibration performed on local starburst galaxies (Meurer et al., 1995, 1999). GALEX observations brought large amount of data in this field since the slope of the UV continuum can be safely deduced from the FUV – NUV color. Studies based on GALEX data have shown that the local starburst calibration is not valid for the bulk of local star forming galaxies (e.g., Dale et al., 2005; Cortese et al., 2006; Boissier et al., 2007; Gil de Paz et al., 2007; Johnson et al., 2007): i.e., these galaxies exhibit lower dust attenuation ($L_{\text{TIR}}/L_{\text{FUV}}$) than expected from their FUV – NUV color. IR selected galaxies also depart from the starburst law but in the opposite way: they are found to exhibit a $L_{\text{TIR}}/L_{\text{FUV}}$ ratio much larger than expected (Buat et al., 2005; Goldader et al., 2002). Here, we re-investigate this issue making use of a much larger sample than used in Buat et al. (2005).

Figure 15 shows the FUV-NUV color against $L_{\text{TIR}}/L_{\text{FUV}}$ (often called the IR-excess (IRX)– β relation) for our sample galaxies together with the local starburst relation. The local relation was taken from Meurer et al. (1999) and converted into the relation between the FUV-NUV color and $L_{\text{TIR}}/L_{\text{FUV}}$ by eqs. (1)

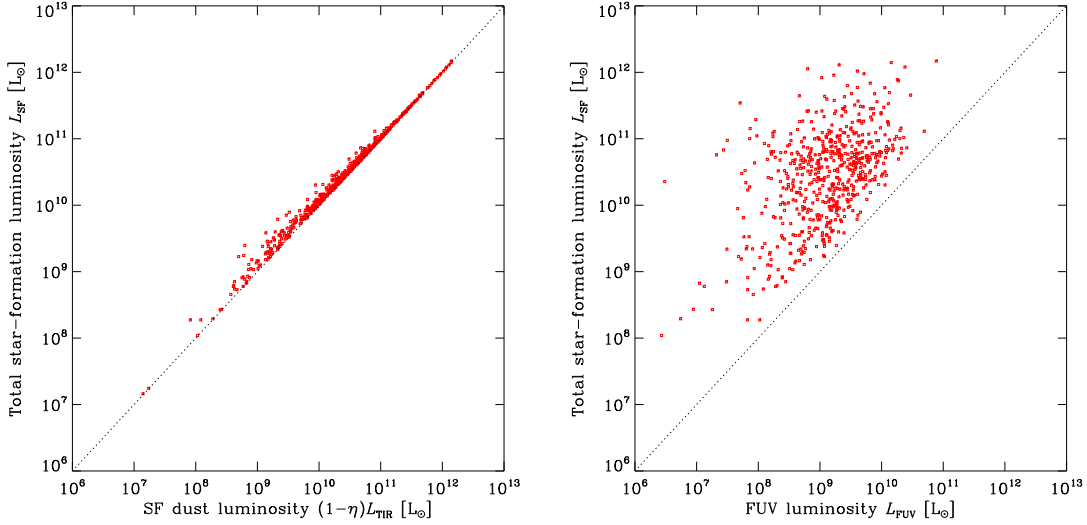


Fig. 12. Contribution of L_{TIR} and L_{FUV} to the total star formation (SF) luminosity L_{SF} , which is the luminosity produced by newly forming stars defined by eq. (13). In the left panel, η is the fraction of IR emission produced by dust heated by old stars which is not related to the current SF (see main text).

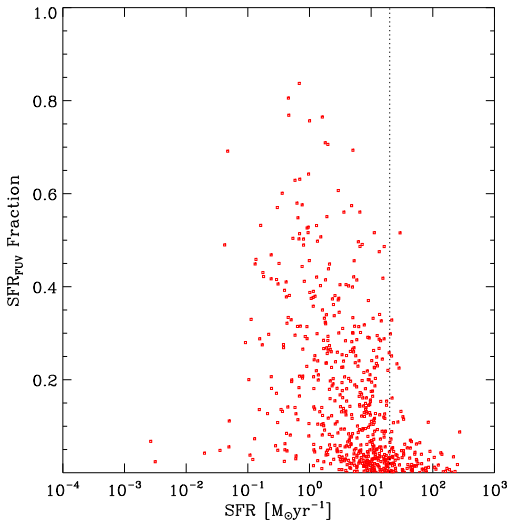


Fig. 13. Contribution of the FUV-estimated (or “directly visible”) SFR, SFR_{FUV} , to the total SFR as a function of total SFR. Vertical dotted line represents the effective boundary above which almost all energy produced by newly forming stars is emitted at IR.

and (2) of Kong et al. (2004):

$$\frac{L_{\text{TIR}}}{L_{\text{FUV}}} = 10^{[1.92(\text{FUV}-\text{NUV})+0.4]} - 0.95. \quad (19)$$

Most of the galaxies lie below the starburst relation by a factor of 5 to 10, but some locate above the relation. A significant fraction of galaxies above the local starburst line are luminous IR galaxies (LIRGs and ULIRGs). Especially, all the ULIRGs have larger $L_{\text{TIR}}/L_{\text{FUV}}$ ratios than expected from the relation. This general trend is quite consistent with Buat et al. (2005). It may be worth mentioning that LIRGs are consistent with the local starburst line. These trends are more clearly represented by functional fits in Right panel of Figure 15. We used a functional

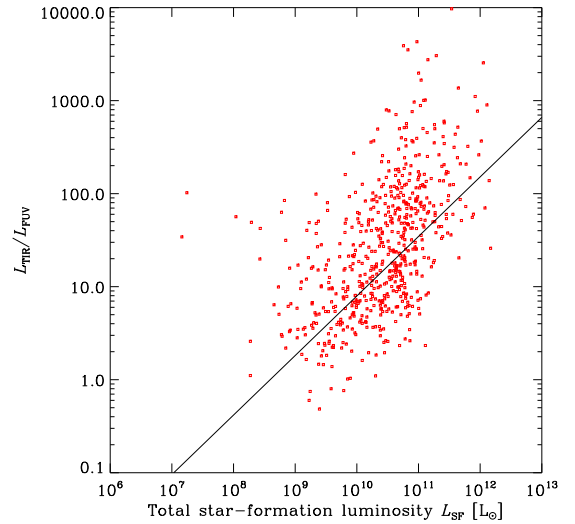


Fig. 14. Distribution of $L_{\text{TIR}}-L_{\text{FUV}}$ ratio as a function of the total star formation luminosity L_{SF} . Solid line is the relation found by IRAS-GALEX analysis (Buat et al., 2007a), represented by eq. (18).

form of eq. (19) for “normal” galaxies with $L_{60} < 10^{11} L_{\odot}$,

$$\frac{L_{\text{TIR}}}{L_{\text{FUV}}} = 10^{[a(\text{FUV}-\text{NUV})+b]} - c. \quad (20)$$

with letting three parameters, a , b and c free. The fitted relation is well below the local starburst relation originally claimed by Meurer et al. (1999). For more luminous galaxies, eq. (20) does not give a reasonable fit, hence we adopted a simple linear fit. Even if LIRGs are roughly consistent with the local starburst relation, the fitted line is much flatter than that, because of the existence of galaxies well above the local starburst line with blue UV color. It is difficult to conclude in the case of ULIRGs because of poor statistics, but the fitted linear relation seems to locate above the local starburst relation. We have seen that galax-

ies with relatively quiescent galaxies ($L_{60} < 10^{11} L_{\odot}$) in our sample locate well below the relation of Meurer et al. (1999). Similar trend was reported for optically selected galaxies (e.g., Boissier et al., 2007; Cortese et al., 2006) Boissier et al. (2007) investigated this relation for normal galaxies selected at optical wavelength with the same functional form with this study [eq. (20)] They found a much flatter relation than Meurer’s original relation, which is presented in Right panel of Figure 15 with dot-dot-dot-dashed line. Cortese et al. (2006) reported a similar result. What is newly clarified in this study is that the same trend is seen for purely FIR-selected sample of SF galaxies. In addition, Boissier et al.’s relation does not represent the relation for our quiescent galaxy sample. This is naturally understood that our sample includes strongly reddened galaxies by dust which can never be picked up by UV-selection.

4.4.3. Attenuation and stellar mass-related quantities

By using optical–NIR flux densities, we can estimate the stellar mass of the sample galaxies. Here we discuss dust attenuation properties with respect to the stellar mass. There are various methods to estimate stellar mass. In this work, we used an SDSS-based method proposed by Yang et al. (2007); these authors assume the Kroupa IMF (Kroupa, 2001), while we used the Salpeter IMF (Salpeter, 1955) to estimate the SFR of galaxies. For consistency, we convert their stellar mass estimates using the conversion factor given by Bell et al. (2003). As for the accuracy of the stellar mass estimates, the relation has been calibrated from SDSS+2MASS data, and the error should be around 20 %. We also estimated the stellar mass from Ks -band using the relations derived by Bell et al. (2003), and the trends did not change significantly. Further exploration for the stellar mass estimation will be discussed elsewhere.

Figure 16 shows the relation between stellar mass M_* and dust attenuation in terms of $L_{\text{TIR}}/L_{\text{FUV}}$. At a first glance, the dependence of dust attenuation on stellar mass is very strong. Though we should be cautious on the selection effect on this plot again, the strong dependence might be partially physical. This implies that larger galaxies are more extinguished. Hence, dust attenuation is closely related to the physical size of galaxies.

The presence of low mass and high $L_{\text{TIR}}/L_{\text{FUV}}$ galaxies $\sim 10\text{--}100$ at $M_* \simeq 10^7\text{--}10^9 M_{\odot}$ is worth mentioning here. Iglesias-Páramo et al. (2006) made essentially the same analysis by GALEX and IRAS. In their studies, such galaxies did not exist in their IR-selected samples (their Figure 12). If the flux measurement is secure, these galaxies deserve a close inspection to examine their nature.

Next, we show the relation between SFR per unit stellar mass, SFR/M_* , which is often referred to as the specific SFR (SSFR), and dust attenuation $L_{\text{TIR}}/L_{\text{FUV}}$ in Figure 17. It is indeed striking that obviously there is no correlation between these quantities.

First conclusion would be that there is no correlation between global attenuation and SSFR. Generally, many authors showed that dust attenuation increases with SFR (see, e.g., Figure 7 of Buat et al., 2007a). Then, if there is no link with the SSFR it implies that dust attenuation is linked to the total amount of SF scaled with galaxy size, because SFR was positively correlated to M_* seen above. It may be interpreted as follows: the attenuation is not related to the current-to-past SFR ratio, or roughly, the SF history. Probably this could be explained by the short lifetime of dust grains in the ISM.

We should mention that, however, Iglesias-Páramo et al. (2006) has shown that even for the FIR-selected galaxies there

is some correlation between these two quantities (see their Figure 10b). This issue seems to require further examination.

5. Conclusion

In order to explore SEDs, star formation, and dust extinction properties of galaxies in the Local Universe, we have constructed a multiband galaxy sample based on the AKARI FIS All-Sky Survey and GALEX All-Sky Imaging Survey (AIS). We start from AKARI All-Sky Survey Bright Source Catalogue β -1.1, and selected galaxies by matching the AKARI sources with those of the IRAS PSCz. Next, we have measured total GALEX FUV and NUV flux densities by a photometry software which we have developed specifically for this purpose. Then, we have matched this sample with SDSS and 2MASS galaxies to obtain the basic sample. The basic sample consists of 776 galaxies. After removing objects with photometry contaminated by foreground sources (mainly in SDSS), we have defined the “secure sample” which contains 607 galaxies. Based on this galaxy sample, we have explored various properties of galaxies related to star formation and dust extinction.

Summary and conclusions of this study are as follows:

1. The sample galaxies have redshifts $\lesssim 0.15$, and their $90\text{-}\mu\text{m}$ luminosities range from 10^6 to $10^{12} L_{\odot}$, with a peak at $10^{10} L_{\odot}$.
2. The SEDs display a very large variety, especially more than four orders of magnitude at M-FIR, but if we sort the sample by $90\text{-}\mu\text{m}$, their average SED has a coherent trend: the more luminous at $90\text{-}\mu\text{m}$, the redder the global SED becomes.
3. The $M_r\text{-NUV} - r$ color-magnitude relation of our sample does not show a bimodality which is almost always expected in optically selected galaxy samples. The distribution is unimodal, centered on the green valley between blue cloud and red sequence seen in optical surveys.
4. We have established formulae to convert FIR luminosity from AKARI bands to the total infrared (IR) luminosity L_{TIR} .
5. The luminosity related to star formation activity (L_{SF}) is dominated by the contribution of L_{TIR} even if we take into account the FIR emission from dust heated by old stars.
6. With these formulae, we calculated the star formation directly visible with FUV and hidden by dust. At high star formation rate (SFR) ($> 20 M_{\odot} \text{yr}^{-1}$), the fraction of directly visible SFR, SFR_{FUV} , decreases.
7. We estimated the ratio, $L_{\text{TIR}}/L_{\text{FUV}}$, which is a direct measure of the FUV attenuation A_{FUV} . The distribution of $L_{\text{TIR}}/L_{\text{FUV}}$ is consistent with a previous result based on GALEX and IRAS (Buat et al., 2007a).
8. We also examined the $L_{\text{TIR}}/L_{\text{FUV}}\text{-UV}$ slope (FUV – NUV) relation. The majority of the sample has $L_{\text{TIR}}/L_{\text{FUV}}$ ratios 5 to 10 times lower than expected from the local starburst relation (Kong et al., 2004), while some LIRGs and all the ULIRGs of this sample have higher $L_{\text{TIR}}/L_{\text{FUV}}$ ratios. This trend was already reported from a previous GALEX-IRAS study (Buat et al., 2005) obtained by a much smaller sample, and we have confirmed their conclusion.
9. By making use of stellar mass information derived from SDSS flux densities in this work, we have examined the dust attenuation properties in terms of stellar mass. We found that the attenuation indicator $L_{\text{TIR}}/L_{\text{FUV}}$ is correlated to stellar mass of galaxies, M_* , but there is no correlation with specific SFR (SSFR), SFR/M_* . This may mean that $L_{\text{TIR}}/L_{\text{FUV}}$ is not linked to the SF history, but simply scales with the size

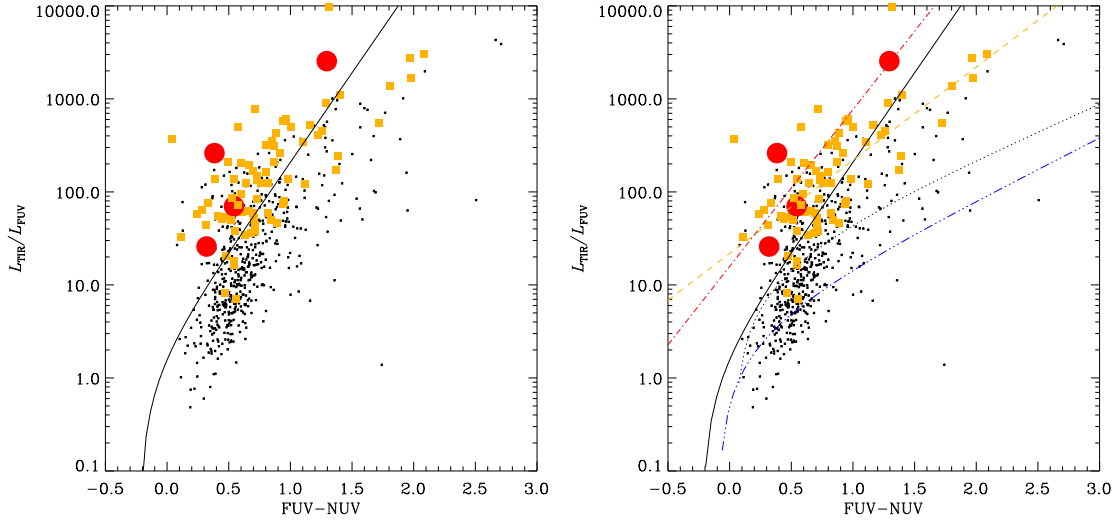


Fig. 15. Distribution of $L_{\text{TIR}}-L_{\text{FUV}}$ luminosity ratio as a function of UV color $\text{FUV} - \text{NUV}$. Dots: galaxies with $60\mu\text{m}$ luminosity $L_{60} < 10^{11} L_{\odot}$, filled squares: galaxies with $10^{11} \leq L_{60} < 10^{12} L_{\odot}$ (IR luminous galaxies: LIRGs), and filled circles: galaxies with $10^{11} \leq L_{60} < 10^{12} L_{\odot}$ (Ultraluminous IR luminous galaxies: ULIRGs). Solid lines in each panel represent the relation between the $\text{FUV}-\text{NUV}$ color [eq. (19)]. Left panel shows the raw distribution of $L_{\text{TIR}}-L_{\text{FUV}}$ luminosity ratio, while in Right panel functional fits are overlotted on the data. For galaxies with $L_{60} < 10^{11} L_{\odot}$, eq. (19) is used, while for more luminous galaxies, simple linear relations are adopted because of poor fit of the function. Dotted line: a fit to galaxies with $L_{60} < 10^{11} L_{\odot}$ by eq. (20); Dot-dot-dot-dashed line: a fit to a sample of normal galaxies by eq. (20) presented by Boissier et al. (2007); Dashed line: a linear fit to LIRGs; Dot-dashed line: a linear fit to ULIRGs.

of galaxies. However, this is at odds with previous result of Iglesias-Páramo et al. (2006).

This sample will serve as an important reference sample at $z = 0$ for various further analysis or ongoing/future observational projects, like Herschel: for instance, this can be used to construct a set of SEDs for discussing higher- z observational strategy, or as a baseline test sample to investigate a method of extracting galaxies only from FIR flux information (e.g., Pollo et al., 2010).

However, since our first sample is not complete in many senses, further analysis will be desired. We plan to construct a larger multiwavelength sample from the next release of AKARI FIS All-Sky Survey in the near future.

Acknowledgements. We deeply thank the anonymous referee for her/his careful reading of the original manuscript, useful suggestions and comments which improved the clarity of the paper. This work is based on observations with AKARI, a JAXA project with the participation of ESA. TTT has been supported by Program for Improvement of Research Environment for Young Researchers from Special Coordination Funds for Promoting Science and Technology, and the Grant-in-Aid for the Scientific Research Fund (20740105) commissioned by the Ministry of Education, Culture, Sports, Science and Technology (MEXT) of Japan. VB and DB have been supported by the Centre National des Etudes Spatiales (CNES) and the Programme National Galaxies (PNG). We thank Agnieszka Pollo, Mai Fujiwara, Akira Ikeyama, Ryosuke Asano, Akio K. Inoue, Hiroshi Shibai, Yasuo Doi, Hideaki Fujiwara, Mitsunobu Kawada, Hidehiro Kaneda, Hiroyuki Hirashita, and Takako T. Ishii for fruitful discussions and comments. TTT, FTY, and KLM are partially supported from the Grand-in-Aid for the Global COE Program “Quest for Fundamental Principles in the Universe: from Particles to the Solar System and the Cosmos” from the MEXT.

References

Bell, E. F., McIntosh, D. H., Katz, N., & Weinberg, M. D. 2003, *ApJS*, 149, 289
 Bell, E. F., et al. 2005, *ApJ*, 625, 23
 Boissier, S., et al. 2007, *ApJS*, 173, 524
 Buat, V., Iglesias-Páramo, J., Seibert, M. et al. 2005, *ApJ*, 619, L51
 Buat, V., Takeuchi, T. T., Iglesias-Páramo, J. et al. 2007a, *ApJS*, 173, 404
 Buat, V., Marcillac, D., Burgarella, D. et al. 2007b, *A&A*, 469, 19

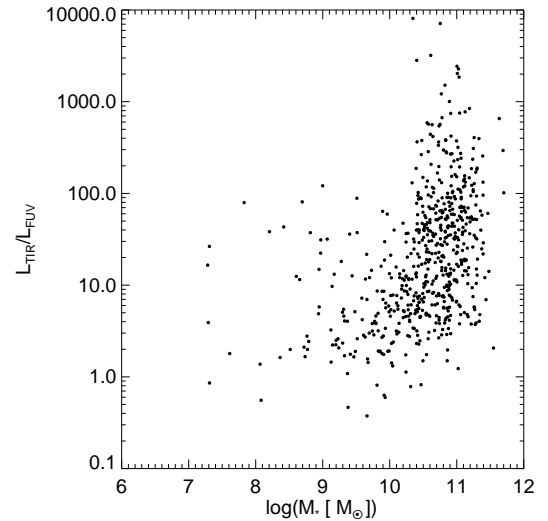


Fig. 16. Relation between stellar mass M_* and dust attenuation indicator $L_{\text{TIR}}/L_{\text{FUV}}$.

Cardelli, J. A., Clayton, G. C., & Mathis, J. S. 1989, *ApJ*, 345, 245
 Chary, R., Elbaz, D. 2001, *ApJ*, 556, 562
 Cortese, L., et al. 2006, *ApJ*, 637, 242
 Dale, D. A., Helou, G., Contursi, A. et al. 2001, *ApJ*, 549, 215
 Dale, D. A., Helou, G. 2002, *ApJ*, 576, 159
 Dale, D. A., Bendo, G. J., Engelbracht, C. W. et al. 2005, *ApJ*, 633, 857
 Daddi, E., et al. 2007, *ApJ*, 670, 156
 Dwek, E., & Scalo, J. M. 1980, *ApJ*, 239, 193
 Dwek, E. 1998, *ApJ*, 501, 643
 Genzel, R., & Cesarsky, C. J. 2000, *ARA&A*, 38, 761
 Gil de Paz, A., et al. 2007, *ApJS*, 173, 185
 Goldader, J. D., Meurer, G., Heckman, T. M., Seibert, M., Sanders, D. B., Calzetti, D., & Steidel, C. C. 2002, *ApJ*, 568, 651

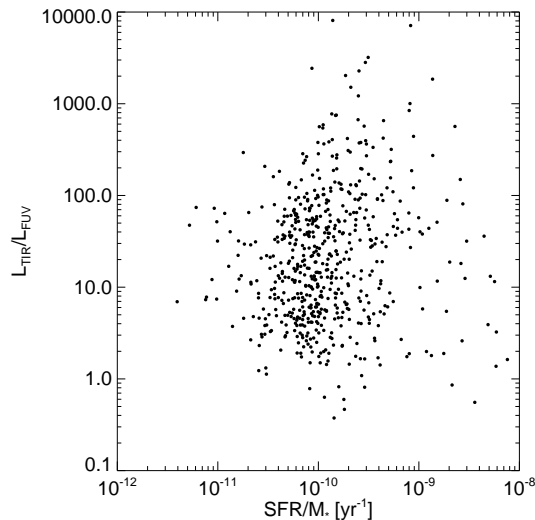


Fig. 17. Relation between SFR per unit stellar mass, SFR/M_* (specific SFR: SSFR), and dust attenuation L_{TIR}/L_{FUV} .

Helou, G., Khan, I. R., Malek, L., & Boehmer, L. 1988, *ApJS*, 68, 151
 Hirashita, H., Buat, V., & Inoue, A. K. 2003, *A&A*, 410, 83
 Hirashita, H., Kaneda, H., Onaka, T., & Suzuki, T. 2008, *PASJ*, 60, 477
 Hopkins, A. M., & Beacom, J. F. 2006, *ApJ*, 651, 142
 Iglesias-Páramo, J., Buat, V., Takeuchi, T. T., et al. 2006, *ApJS*, 164, 38
 Jarrett, T. H., Chester, T., Cutri, R., Schneider, S., Skrutskie, M., & Huchra, J. P. 2000, *AJ*, 119, 2498
 Jeong, W.-S., et al. 2007, *PASJ*, 59, 429
 Johnson, B. D., et al. 2007, *ApJS*, 173, 377
 Kartaltepe, J. S., et al. 2009, *Astronomical Society of the Pacific Conference Series*, 408, 272
 Kawada, M., et al. 2007, *PASJ*, 59, 389
 Kong, X., Charlot, S., Brinchmann, J., & Fall, S. M. 2004, *MNRAS*, 349, 769
 Kroupa, P. 2001, *MNRAS*, 322, 231
 Martin, D. C., et al. 2005, *ApJ*, 619, L1
 Martin, D. C., et al. 2007, *ApJS*, 173, 342
 Meurer, G. R., Heckman, T. M., & Calzetti, D. 1999, *ApJ*, 521, 64
 Meurer, G. R., Heckman, T. M., Leitherer, C., Kinney, A., Robert, C., & Garnett, D. R. 1995, *AJ*, 110, 2665
 Morrissey, P., et al. 2007, *ApJS*, 173, 682
 Murakami, H., et al. 2007, *PASJ*, 59, 369
 Nozawa, T., Kozasa, T., Umeda, H., Maeda, K., & Nomoto, K. 2003, *ApJ*, 598, 785
 Onaka, T., et al. 2007, *PASJ*, 59, S401
 Pollo, A., Rybka, P., & Takeuchi, T. T. 2010, *A&A*, submitted to this volume
 Neugebauer, G., et al. 1984, *ApJ*, 278, L1
 Reddy, N. A., Steidel, C. C., Pettini, M. et al. 2008, *ApJS*, 175, 48
 Reddy, N. A., & Steidel, C. C. 2009, *ApJ*, 692, 778
 Salim, S., et al. 2007, *ApJS*, 173, 267
 Salpeter, E. E. 1955, *ApJ*, 121, 161
 Sanders, D. B., & Mirabel, I. F. 1996, *ARA&A*, 34, 749
 Saunders, W., et al. 2000, *MNRAS*, 317, 55
 Schlegel, D. J., Finkbeiner, D. P., & Davis, M. 1998, *ApJ*, 500, 525
 Seibert, M., et al. 2005, *ApJ*, 619, L55
 Skrutskie, M. F., et al. 2006, *AJ*, 131, 1163
 Soifer, B. T., Houck, J. R., & Neugebauer, G. 1987, *ARA&A*, 25, 187
 Soifer, B. T., Helou, G., & Werner, M. 2008, *ARA&A*, 46, 201
 Takeuchi, T. T., Hirashita, H., Ohta, K., Hattori, T. G., Ishii, T. T., & Shibai, H. 1999, *PASP*, 111, 288
 Takeuchi, T. T., Ishii, T. T., Hirashita, H., Yoshikawa, K., Matsuhara, H., Kawara, K., & Okuda, H. 2001, *PASJ*, 53, 37
 Takeuchi, T. T., Kawabe, R., Kohno, K., Nakanishi, K., Ishii, T. T., Hirashita, H., & Yoshikawa, K. 2001, *PASP*, 113, 586
 Takeuchi, T. T., Yoshikawa, K., & Ishii, T. T. 2003, *ApJ*, 587, L89
 Takeuchi, T. T., Hirashita, H., Ishii, T. T., Hunt, L. K., & Ferrara, A. 2003, *MNRAS*, 343, 839
 Takeuchi, T. T., & Ishii, T. T. 2004, *ApJ*, 604, 40
 Takeuchi, T. T., Buat, V., Burgarella, D. 2005a, *A&A*, 440, L17

Takeuchi, T. T., Buat, V., Iglesias-Páramo, J., Boselli, A., Burgarella, D. 2005b, *A&A*, 432, 423
 Takeuchi, T. T., Ishii, T. T., Nozawa, T., Kozasa, T., & Hirashita, H. 2005c, *MNRAS*, 362, 592
 Vergani, D., et al. 2009, arXiv:0909.1968
 Verma, A., Charmandaris, V., Klaas, U., Lutz, D., & Haas, M. 2005, *Space Science Reviews*, 119, 355
 Yamamura, I., et al. 2009 in *AKARI, a light to illuminate the misty Universe*, eds. T. Onaka, G. White, T. Nakagawa, I. Yamamura, ASP Conf. Ser., in press
 Yamamura, I., Fukuda, Y., & Makiuti, S. 2008, *AKARI/FIS All-Sky Survey Bright Source Catalogue Version β -1 Release Note (Rev. 1)*
 Yang, X., Mo, H. J., van den Bosch, F. C., Pasquali, A., Li, C., & Barden, M. 2007, *ApJ*, 671, 153
 Zheng, X. Z. et al. 2006, *ApJ*, 640, 784

Appendix A: Luminosity vs. redshift diagrams of the sample

In Appendix, we show the redshift–luminosity relations for all the bands we have used in the main text (Fig. A.1). These plots help to examine the effect of the selection functions of our sample at each band.

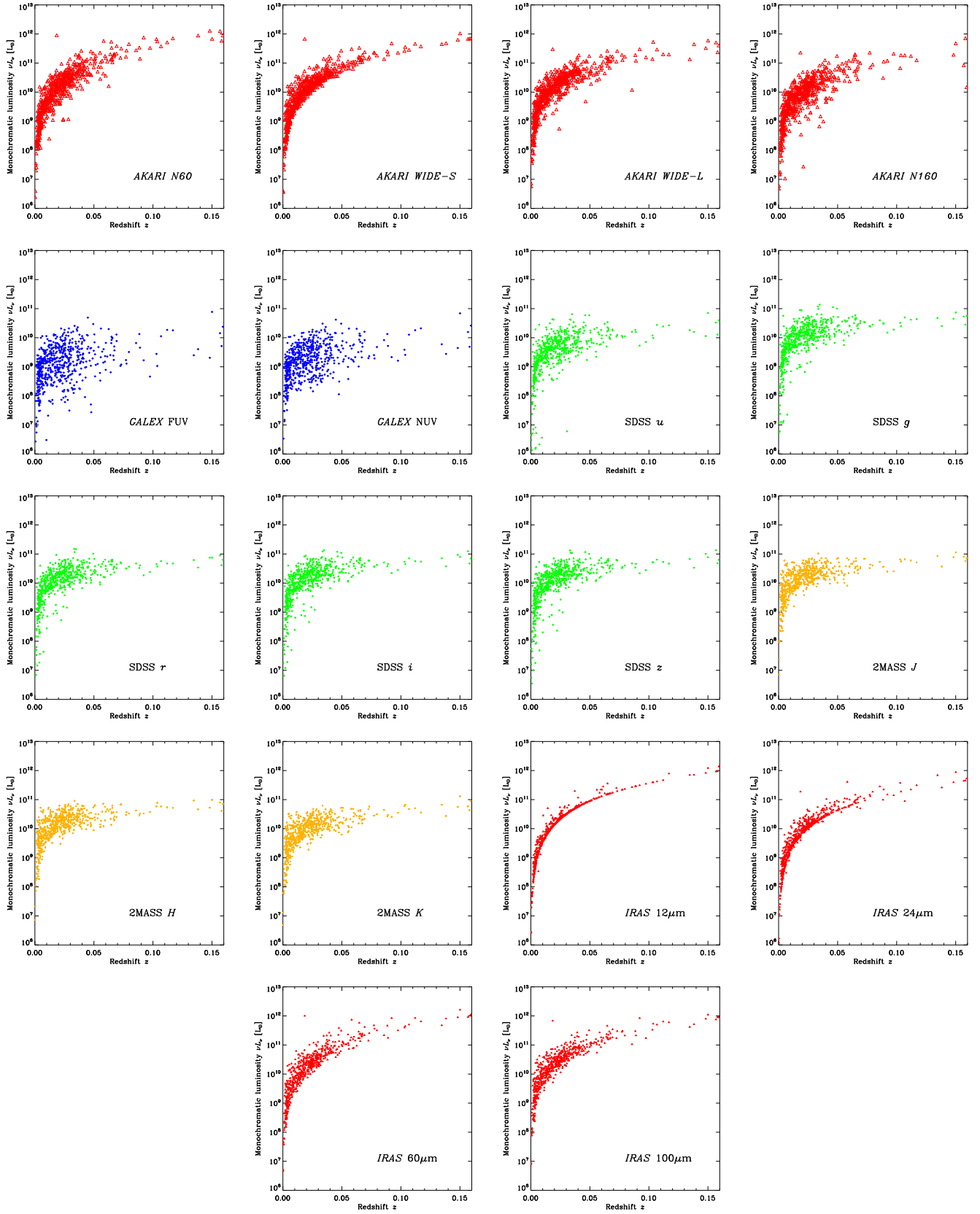


Fig. A.1. Luminosity vs. redshift diagrams for all the bands in the sample.